Control of High Quality SrVO3 Electrode in Oxidizing Atmosphere

B. Bérini, Valérie Demange, M. Bouttemy, E. Popova, N. Keller, Y. Dumont, A. Fouchet

Control of High Quality $SrVO_3$ Electrode in Oxidizing Atmosphere

B. Bérini, V. Demange, M. Bouttemy, E. Popova, N. Keller, Y. Dumont and A. Fouchet**

Dr. B. Bérini, Dr. E. Popova, Dr. N. Keller, Prof. Y. Dumont and Dr. A. Fouchet**

Groupe d'Étude de la Matière Condensée (UMR 8635) Université de Versailles Saint-Quentin-en-Yvelines - CNRS- Université Paris-Saclay, 45 Av. des États-Unis; 78035 Versailles; France

Dr. V. Demange

Institut des Sciences Chimiques de Rennes, (UMR CNRS 6226) Université de Rennes 1, Campus de Beaulieu, 35042 Rennes Cedex; France

Dr. M. Bouttemy

Institut Lavoisier de Versailles, (UMR 8180) Université de Versailles-Saint-Quentin-en-Yvelines - CNRS- Université Paris-Saclay, 45 Av. des États-Unis 78035 Versailles; France

E-mail: bruno.berini@uvsq.fr, arnaud.fouchet@uvsq.fr

Keywords: pulsed laser ablation, perovskites, surface oxidation

$SrVO_3$ (SVO) is a model system for strongly correlated oxides and is highly promising as conductive layer in heterostructures. Therefore, the control of electronic properties and morphology are essential for the advanced applications. Here, we explore the oxygen stability during and after the deposition, as SVO film is expected to undergo different post-deposition thermal and atmosphere treatments during its integration in a heterostructure. Hence, the influence of oxygen stability on morphology and electrical properties of the metallic $SrVO_3$ grown by pulsed laser deposition has been investigated. Films grown under vacuum ($SrVO_{3-\delta}$) exhibit a very smooth surface while films grown under higher oxygen pressure roughen and present nanostructures at the surface. These nanostructures are found to be of $Sr_3V_2O_8$ phase and their apparition can be controlled by the oxygen supply. Subsequent thermal treatments at different temperatures under same oxygen pressure prevent formation of the $Sr_3V_2O_8$ phase, lead to the stoichiometric $SrVO_3$ and thus improve the transport properties. In this study is shown the extreme sensitivity of SVO to oxygen and the conditions to obtain high quality smooth SVO films with improved electrical properties for electrode application.

1. Introduction

Transition metal oxides with the perovskite structure have attracted a growing interest these last decades due to their exceptionally broad range of versatile functionalities arising from the complex interplay between charge, orbital, spin and lattice degrees of freedom and controllable by external stimuli (electric/magnetic fields, light, stress, …). These functionalities open the way for many modern applications of perovskites in the field of oxitronics, such as for example switches or sensors [1–4].

This class of materials presents a wide panel of properties and phenomena (insulator to superconductor, metal-insulator transition, ferroelectricity, magnetism, multiferroicity…[1]). Among the perovskites, strontium vanadate $SrVO_3$ (SVO) combines the advantages of relative simple cubic structure (space group *Pm-3m*, *a*=0.3843 nm) with only one electron per vanadium. As a model for correlated system, its electronic structure is widely studied by angle-resolved photoemission spectroscopy (ARPES) experiments supported by theoretical calculations [5–7]. SVO is thus a model system for studying fundamental phenomenon in condensed matter physics like the metal-insulator transition (MIT) [8–10]. Different approaches have been adopted to induce the MIT in perovskites, such as bandwidth control using chemical doping [11,12] or a dimensional crossover–driven MIT by reducing the thickness under 2-3 monolayers [9].

Due to its excellent electrical conductivity, SVO (and its derivatives Ca, Y or Al substituted SVO) is also a promising candidate for solid oxide fuel cell anodes [13], can serve as an epitaxial conducting electrode in all oxide heterostructures [14–16] or has been recently proposed to be used as a transparent conductor [17]. Nevertheless, SVO is sensitive to oxygen atmosphere and V^{4+} has the tendency to dismutation [18]. High quality of materials depositions, perfect control of the roughness and maintaining physical properties during the whole integration processes are the keys components towards the realization of functional material heterostructures. While other strongly correlated electrons perovskite electrodes ($SrRuO_3$ or $LaNiO_3$) are grown under high oxygen pressure conditions [19–21] and easily unstable in vacuum, SVO has the specificity to be grown under low

oxygen pressures, opening the possibility for exploring new heterostructures. Due to these applications of SVO as conductive layers, it is of importance to control its electrical properties and study its stability in oxidizing atmosphere at high temperature. In this work, we study this stability, identifying formation of phases under certain conditions, finding a way to optimize by post-annealing treatment the electrical properties of the SVO layer.

In the following, the properties of three relevant samples will be discussed in details. The first sample, labelled "a", was grown under vacuum ($1x10^{-5}$ Pa), the second one ("b") in an oxygen pressure of $1.2x10^{-4}$ Pa. The cooling down of both films was done at the deposition pressure. The sample "c" grew under an oxygen pressure of $1.2x10^{-4}$ Pa and cooled in vacuum.

2. Results and Discussion

2.1 Films morphology

SVO compound is particularly sensitive to oxygen pressure (PO_2) [13,22,23]. Sample "a" crystallized in vacuum presents an increase of the out-of-plane lattice parameter to 0.3896 nm, compared to the bulk value. This expansion can be interpreted considering the presence of oxygen vacancies which increase the volume of the unit cell and is a general behaviour in perovskite oxide [24,25]. Each oxygen vacancy donates 2 electrons to the neighbouring d-orbitals of vanadium reducing the vanadium from V^{4+} to V^{3+} and increasing the ionic radius of the vanadium ion[26]. For film grown at PO_2 = $1.2x\ 10^{-4}$ Pa (film "b"), 0.3836 nm out-of-plane and 0.3891 nm in-plane parameters were measured for the epitaxial SVO by reciprocal space X-ray diffraction (XRD) mapping of (002), (103) and (-103) reflections (Bruker D8 Discover*)* and no additional phases were detected in the probed area ((see fig. SI1, SI2)).

As can be seen on the fig. SI2 (a), at this thickness (100 nm), some relaxation occurs, which can explained why the c lattice parameter is a little larger than expected for SVO film deposited on STO.

For the films grown at oxygen pressure above $5x10^{-2}$ Pa, the $Sr_2V_2O_7$ phase is also present and corresponds to a higher oxidation state of vanadium from V^{4+} (SVO) to V^{5+}.

Figures 1a and 1b present AFM images of samples "a" and "b", respectively. At the lowest pressure, the sample presents a very smooth morphology with a root mean square (RMS) roughness of 0.3 nm, whereas for the film deposited at $1.2x10^{-4}$ Pa a RMS roughness of 4.3 nm is measured and its surface presents self-organized oblong nanostructures that are oriented along the two <011> directions of the STO substrate with two different variants (tip sweeping parallel to the STO [010] direction). As these nanostructures induce a roughening of the film surface and do not appear in film elaborated in vacuum, attempt to optimise the morphology was done by suppressing the supply of oxygen just after the deposition at $1.2x10^{-4}$ Pa (film “c”). Interestingly, the roughness of this film reduces to a RMS roughness of 0.3 nm (Figure 1c) which is the same as for the film elaborated in vacuum. We can conclude from these experiments that the appearance of such nanostructures is related to the post-deposition process rather than to the growth itself.

2.2 NanoAuger measurements and Transmission electronic microscopy

In order to understand the apparition of these nanostructures, nano-Auger measurements (nano-AES) and TEM have been carried out. For nano-AES, the purpose was to determine if the cationic stoichiometry of the nanocrystallites differs from the one of the SVO matrix. Thanks to its surface sensitivity and nanometric resolution inferior to the patterning dimensions, the composition difference of nanocrystallites and SVO could be investigated. The beam positioning was controlled by using a probe tracking tool to correct possible drift during acquisition. The AES widescans spectra obtained in both specific locations (Figure 2) show similar qualitative information with a minor C contamination layer at the surface and the Auger transitions of the constitutive elements Sr, V and O. The spatial distribution of Sr and V in a restricted area around 2 nanocrystallites was studied using the main Sr-LMM (1642 eV) and V-MVV (469 eV) transitions to image the intensities

variation. SAM images (figure 2a) evidence a slight intensity contrast modification between the SVO matrix and the nanostructures agreeing for a small Sr enrichment in the nanostructures and consequently a lower amount of vanadium. Topographic origin of this intensity change is unlikely as the Auger electron escape depth (4 nm) is equivalent to the thickness of the structures. In addition, even if it remains difficult to obtain quantitatively the cationic ratio Sr/V, especially at this high precision level, a slight Sr/V modulation of the intensities ratio from 0.65 (matrix) to 0.70 (nano-structure) was determined from point analyses (Figure 2b), confirming the SAM results.

Structural properties of the nanoparticles were investigated by TEM measurements. In supplementary information, Figure SI3 shows a HRTEM of $Sr_3V_2O_8$ nanostructures onto $SrVO_3$ of the sample "b" and Figure 3a presents an electron diffraction pattern (EDP) containing substrate, film and nanostructure along the STO [100] zone axis. For EDP, no reflection of the SVO film is observed, because the in-plane parameter of SVO (0.3891 nm) is very close to the one of STO (0.3905 nm) and cannot be separated. In addition to the substrate reflections, one can observed additional spots that were attributed to the $Sr_3V_2O_8$ phase oriented along the [-552] zone axis (space group *R-3m*; hexagonal lattice parameters a = 0.5619 nm, c = 2.0108 nm). This orientation corresponds to the (103) plane oriented almost parallel to the surface (the angle between [-552] direction and the (103) plane is close to 90°, i.e. 86.4°). Two variants of this phase, rotated of 90° from each other, are simultaneously observed as schemed in figure 3b (by using CaRine and CrystalMaker softwares), with the coincidence of the {011} reflections of STO with the {110} reflections of the $Sr_3V_2O_8$ phase. The orientation relationships between the $Sr_3V_2O_8$ phase and the substrate were determined as being:

(110) $Sr_3V_2O_8$ // (011) STO

(-11-5) $Sr_3V_2O_8$ // (01-1) STO

[-552] $Sr_3V_2O_8$ // [100] STO

The structure of $Sr_3V_2O_8$ displays an anisotropic cell along the [-552] zone axis that is related to the anisotropic form of the nanostructures (Fig. SI4). Scheme of [-552]-oriented $Sr_3V_2O_8$ structure onto the STO structure shows a (110) $Sr_3V_2O_8$ spacing (d(110) = 2.81 Å) nearly equal to that of (011) STO (d(011) = 2.761 Å), resulting in an excellent epitaxial match (Fig.SI4). Tilting of the film in the TEM allows to observe other EDPs in zone axis showing other reflections of the $Sr_3V_2O_8$ phase (fig.SI5).

Apparition of the nanostructures on top of the SVO film is an oxidation process which is inversed to what was observed by Macias *et al*. [23] at high temperature (900°C) suggesting a reduction reaction path from pyrovanadate phase ($Sr_2V_2O_7$) to $SrVO_{3-\delta}$ expressed as:

$$8Sr_2V_2O_7 \xrightarrow{-2.5O_2} 5Sr_3V_2O_8 + SrV_6O_{11} \xrightarrow{-\chi O_2} 16SrVO_{3-\delta}$$

In our case, SVO decomposes into a main orthovanadate ($Sr_3V_2O_8$) and SrV_6O_{11} minority phase mixture in oxidizing atmosphere of $1x10^{-4}$ Pa. As the oxygen pressure is low, the SVO films are partially oxidized and only high oxygen pressure above $5x10^{-2}$ Pa oxidizes fully the vanadate phase to $Sr_2V_2O_7$ [23]. This process occurs when V^{4+} is oxidized in V^{5+} with a phase transformation of perovskite $SrVO_3$ into orthovanadate $Sr_3V_2O_8$. This new phase is epitaxed on $SrVO_3$ surface and due to lattice mismatch and crystallographic orientations between both materials, two variants appears as shown by TEM and AFM analysis.

2.3. Electrical Transport Properties

Transport measurements have been performed for the films in the temperature range [2 K-300 K] and are presented in figure 4. All the samples show a decrease of the resistivity with decreasing temperature which is characteristic of metallic behaviour. A resistivity of 4.10^{-5} ohm.cm at room temperature corresponds to a state-of-art value for samples elaborated by PLD on STO[27–31]. By comparison, samples grown in vacuum $1.0x10^{-5}$ Pa (“a”) and in $1.2x10^{-4}$ Pa of O_2 pressure

("b"), present a R_{300K}/R_{10K}= 1.77 and 2.43, respectively. We can notice that the film "b" grown under $1.2x10^{-4}$ Pa in spite of the presence of the nanostructures at the surface, is also a better conductor than the film synthetized in vacuum ("a"). It means that conductivity is directly bound to the oxygen deficiency. The film "c", grown at $1.2x10^{-4}$ Pa and cooled in vacuum, presents a R_{300K}/R_{10K} = 1.76 which is comparable to the film grown in vacuum. Furthermore, resistivity follows a quadratic temperature dependence $\rho = \rho_0 + A * T^2$ characteristic of a Fermi liquid behaviour commonly observed for strongly correlated electron perovskites as seen in the inset of figure 4. In this dependence, ρ_0 is the background contribution due to static disorder and the parameter *A* is related to electron-electron scattering. The different parameters are reported in the table 1. Interestingly when the film is grown at $1.2x10^{-4}$ Pa ("b"), the static disorder is lower than for the films "a" and "c". This static disorder seems to be related to the presence of oxygen vacancies which can act as scattering centers. Furthermore, the parameter *A* related to the electron-electron scattering increases when the amount of oxygen vacancies is reduced. This could be explained by the modification of the Fermi surface. Since *A* is proportional to the square of the effective mass m^{*2} and also to the Fermi wave-vector k_F, a small variation of the shape of the Fermi surface due to the structural distortion may lead to changes in *A* as seen when Ca is substituted by Sr in $Ca_{1-x}Sr_xVO_3$ [11]. This can be explained by the increase of the unit cell from 0.3836 nm to 0.3896 nm induced by the presence of the oxygen vacancies.

2.4. Post thermal treatments

From these findings, the challenge for applications is to combine good electrical properties with a flat surface. To achieve this goal, several thermal treatments consisting of one hour heating/two hours plateau/20 minutes cooling cycle were performed in an oxidizing atmosphere ($1.2x10^{-4}$ Pa) at several temperatures in the range [230-730°C] (steps 1-6). During a subsequent step, oxygen was introduced at high temperature (step 7). Figure 5 combines the transport measurements and **s**urface

roughness, as a measurement of the nanostructures formation at each step. The roughness increases slightly after the first step and remains constant (around 1 nm) without apparition of nanostructures. In addition, an improvement of electrical properties happened at step 5, for a temperature above 600°C, and becomes close to the best value at 730°C, confirming the possibility to obtain well-oxidized SVO films with a flat surface. Surprisingly, thermal treatment at 730°C, e.g. close to the growth temperature does not lead to formation of nanostructures. Two other cycles at 730°C under higher oxygen pressure ($1x10^{-3}$ Pa and $1x10^{-2}$ Pa) have been realized (step 8 and 9). The result is the apparition of nanostructures, evidencing the role of the oxygen pressure. Finally, when the film is annealed under a pressure of $1x10^{-2}$ Pa (step 9), it becomes insulating (non-measurable by PPMS setup) with the transformation of the SVO phase into $Sr_2V_2O_7$ phase (evidenced by XRD: see figure SI6) and its RMS roughness value is 35 nm. These results are consistent with thermogravimetric analysis where oxidation of $SrVO_{3-d}$ in air with temperature shows two transitions: a complete oxidation of V^{3+} to V^{4+} corresponding to stoichiometric SVO_3 and a second transition at higher temperature the oxidation of V^{4+} to V^{5+}, leading to $Sr_2V_2O_7$[13]. Improvements of the static disorder from compensation of oxygen vacancies can also be observed for these films where the ρ_0 decreases from 3 to $1.58x10^{-5}$ ohm.cm, which is close to the value of film "b" (see table 1). The A factor tends to increase slightly with the reoxygenation. This is related to the change of the structural distortion as well. Indeed, in case of a reoxygenation, we observe the decrease of the c parameter from 0.3896 to 0.3841 nm at step 7 and 8, close to the value of the "b" film, e.g. a more stoichiometric SVO film. Finally, we show that the film can be reoxidized without apparition of nanostructures at temperature of 630°C and above. We can deduce that the nanostructures appear at the temperature of growth and with oxygen pressure higher than $1.2x10^{-4}$ Pa.

3. Conclusions

In conclusion, SVO can be grown with very smooth surface even to the thicknesses around 100 nm and can be used as electrodes for heteroepitaxial growth of complex oxides or heterostructures. Nevertheless, we show that this material is unstable when oxygen pressure is increased at high temperature. Self-organized nanostructures of $Sr_3V_2O_8$ are identified to form on top of the films depending on the PO_2 and the temperature which drastically modifies the surface roughness. In order to prevent the apparition of these nanostructures, the film must be kept at oxygen pressure lower than $P=1.2x10^{-4}$ Pa at 750°C. The electrical properties are clearly associated to oxygen vacancies and a post-annealing treatment in the temperature range [600°C – 730°C] allows a better reoxygenation. These temperature and pressure define the stability and post-annealing region of the SVO films to take into account for growth processes of "all oxide heterostructures" with high quality electric properties. SVO takes a complementary place with respect to $SrRuO_3$ or $LaNiO_3$ as electrode brick in "all oxide heterostructures" because of its stability region under low oxygen pressure.

4. Experimental Section

Films of SVO have been grown by pulsed laser deposition (PLD) on single-crystal (SurfaceNet GmbH) $SrTiO_3$ (100) (STO) substrates (10 x 10 x 0.5 mm^3). The lattice mismatch between films and substrates introduces 1.6 % tensile planar strain. A KrF excimer laser (λ = 248 nm) at a fluency of 1.85 J/cm² and 2 Hz repetition rate was used in the PLD setup. The base pressure of the chamber is 5 10^{-7} Pa and the distance between target and substrate is 5 cm. The temperature is fixed at 760°C while different oxygen pressures from $1x10^{-5}$ to $1x10^{-1}$ Pa) were investigated. Film thicknesses of approximatively 100 nm have been determined by conventional step-meter measurements (Bruker Dektak 8). Topography and roughness of the films have been investigated by atomic force microscopy (AFM) (Bruker Dimension 3100) in tapping mode using commercial tips with 300 kHz resonant frequency and 40 N/m spring constant. Transport properties were measured using four in-

line aluminium pad contact geometry in a Physical Properties Measurement System (PPMS) in the 2K-300K temperature range.

The surface composition was analysed at nanometric scale using a new generation Auger nanoprobe (Jeol JAMP 9500F) whose lateral resolution (12 nm spot size) enables to separately characterize the $SrVO_3$ film and the nanostructures. Scanning Auger microscopy (SAM) was additionally performed to map the elements distribution at the surface.

Transmission electron microscopy (TEM) study of the film "b" was performed by using a Jeol 2100 instrument. Fraction of sample containing substrate, film and nanostructures were deposited through random sampling on a commercial carbon-coated copper microgrid. High resolution TEM (HRTEM) images were performed on film and nanostructures under weak illumination to prevent irradiation damages on SVO film.

[1] P. Zubko, S. Gariglio, M. Gabay, P. Ghosez, J.-M. Triscone, *Annu. Rev. Condens. Matter Phys.* **2011**, *2*, 141.
[2] E. Y. Tsymbal, E. R. A. Dagotto, C.-B. Eom, R. Ramesh, *Multifunctional Oxide Heterostructures*, OUP Oxford, **2012**.
[3] J. Chakhalian, J. W. Freeland, A. J. Millis, C. Panagopoulos, J. M. Rondinelli, *Rev. Mod. Phys.* **2014**, *86*, 1189.
[4] M. Bibes, J. E. Villegas, A. Barthélémy, *Adv. Phys.* **2011**, *60*, 5.
[5] M. Takizawa, M. Minohara, H. Kumigashira, D. Toyota, M. Oshima, H. Wadati, T. Yoshida, A. Fujimori, M. Lippmaa, M. Kawasaki, H. Koinuma, G. Sordi, M. Rozenberg, *Phys. Rev. B* **2009**, *80*, 235104.
[6] K. Yoshimatsu, K. Horiba, H. Kumigashira, T. Yoshida, A. Fujimori, M. Oshima, *Science* **2011**, *333*, 319.
[7] S. Backes, T. C. Rödel, F. Fortuna, E. Frantzeskakis, P. Le Fèvre, F. Bertran, M. Kobayashi, R. Yukawa, T. Mitsuhashi, M. Kitamura, K. Horiba, H. Kumigashira, R. Saint-Martin, A. Fouchet, B. Bérini, Y. Dumont, A. J. Kim, F. Lechermann, H. O. Jeschke, M. J. Rozenberg, R. Valentí, A. F. Santander-Syro, *Submitt. PRL ArXiv160206909v1* **2016**.
[8] B. Berini, N. Keller, Y. Dumont, E. Popova, W. Noun, M. Guyot, J. Vigneron, A. Etcheberry, N. Franco, R. M. C. da Silva, *Phys. Rev. B* **2007**, *76*, DOI 10.1103/PhysRevB.76.205417.
[9] K. Yoshimatsu, T. Okabe, H. Kumigashira, S. Okamoto, S. Aizaki, A. Fujimori, M. Oshima, *Phys. Rev. Lett.* **2010**, *104*, 147601.
[10] B. Berini, N. Keller, B. Pigeau, Y. Dumont, E. Popova, N. Franco, R. M. C. da Silva, *J. Appl. Phys.* **2008**, *104*, 103539.
[11] I. H. Inoue, O. Goto, H. Makino, N. E. Hussey, M. Ishikawa, *Phys. Rev. B* **1998**, *58*, 4372.
[12] I. H. Inoue, H. Makino, I. Hase, M. Ishikawa, N. E. Hussey, M. J. Rozenberg, *Phys. B Condens. Matter* **1997**, *237*, 61.
[13] A. A. Yaremchenko, B. Brinkmann, R. Janssen, J. R. Frade, *Solid State Ion.* **2013**, *247–248*, 86.
[14] J. A. Moyer, C. Eaton, R. Engel-Herbert, *Adv. Mater.* **2013**, *25*, 3578.
[15] C. Eaton, J. A. Moyer, H. M. Alipour, E. D. Grimley, M. Brahlek, J. M. LeBeau, R. Engel-Herbert, *J. Vac. Sci. Technol. A* **2015**, *33*, 061504.
[16] M. Brahlek, L. Zhang, C. Eaton, H.-T. Zhang, R. Engel-Herbert, *Appl. Phys. Lett.* **2015**, *107*, 143108.
[17] L. Zhang, Y. Zhou, L. Guo, W. Zhao, A. Barnes, H.-T. Zhang, C. Eaton, Y. Zheng, M. Brahlek, H. F. Haneef, N. J. Podraza, M. H. W. Chan, V. Gopalan, K. M. Rabe, R. Engel-Herbert, *Nat. Mater.* **2015**, *15*, 204.
[18] P. Dougier, P. Hagenmuller, *J. Solid State Chem.* **1975**, *15*, 158.
[19] H. N. Lee, H. M. Christen, M. F. Chisholm, C. M. Rouleau, D. H. Lowndes, *Appl. Phys. Lett.* **2004**, *84*, 4107.
[20] G. Rijnders, D. H. A. Blank, J. Choi, C.-B. Eom, *Appl. Phys. Lett.* **2004**, *84*, 505.
[21] B. Berini, W. Noun, Y. Dumont, E. Popova, N. Keller, *J. Appl. Phys.* **2007**, *101*, 023529.
[22] Z. Cheng, S. Zha, L. Aguilar, M. Liu, *Solid State Ion.* **2005**, *176*, 1921.
[23] J. Macías, A. A. Yaremchenko, J. R. Frade, *J. Alloys Compd.* **2014**, *601*, 186.
[24] B. L. Chamberland, P. S. Danielson, *J. Solid State Chem.* **1971**, *3*, 243.
[25] A. P. Chen, F. Khatkhatay, W. Zhang, C. Jacob, L. Jiao, H. Wang, *J. Appl. Phys.* **2013**, *114*, 124101.
[26] R. t Shannon, *Acta Crystallogr. A* **1976**, *32*, 751.
[27] M. Gu, S. A. Wolf, J. Lu, *Adv. Mater. Interfaces* **2014**, *1*, 1300126.
[28] H. Koinuma, M. Yoshimoto, H. Nagata, T. Tsukahara, *Solid State Commun.* **1991**, *80*, 9.
[29] W. C. Sheets, B. Mercey, W. Prellier, *Appl. Phys. Lett.* **2007**, *91*, 192102.
[30] H. Nagata, T. Tsukahara, M. Yoshimoto, H. Koinuma, *Thin Solid Films* **1992**, *208*, 264.
[31] D. H. Kim, D.-W. Kim, B. S. Kang, T. W. Noh, D. R. Lee, K.-B. Lee, S. J. Lee, *Solid State Commun.* **2000**, *114*, 473.

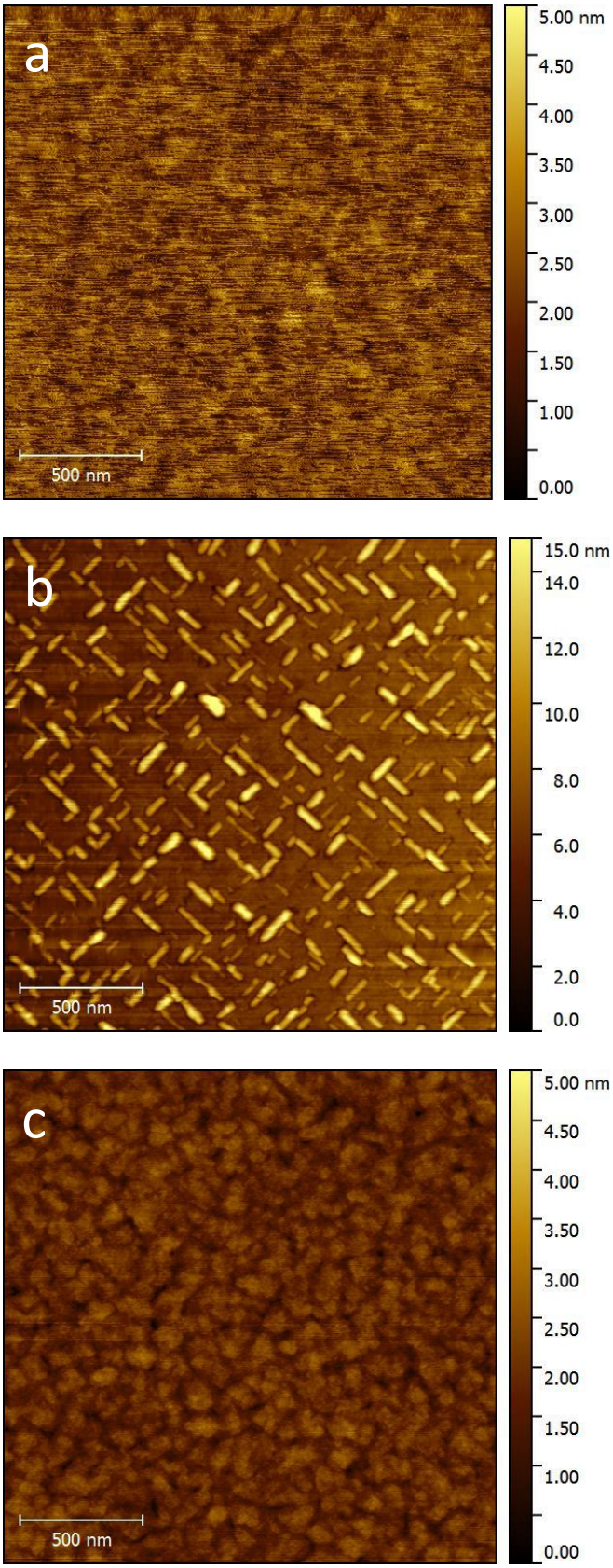

Figure 1. AFM images for the three samples, grown at PO_2= 1x10^{-5} Pa, "a" and 1.2x10^{-4} Pa, "b", grown at PO_2= 1.2x10^{-4} Pa and cooled in vacuum,"c"

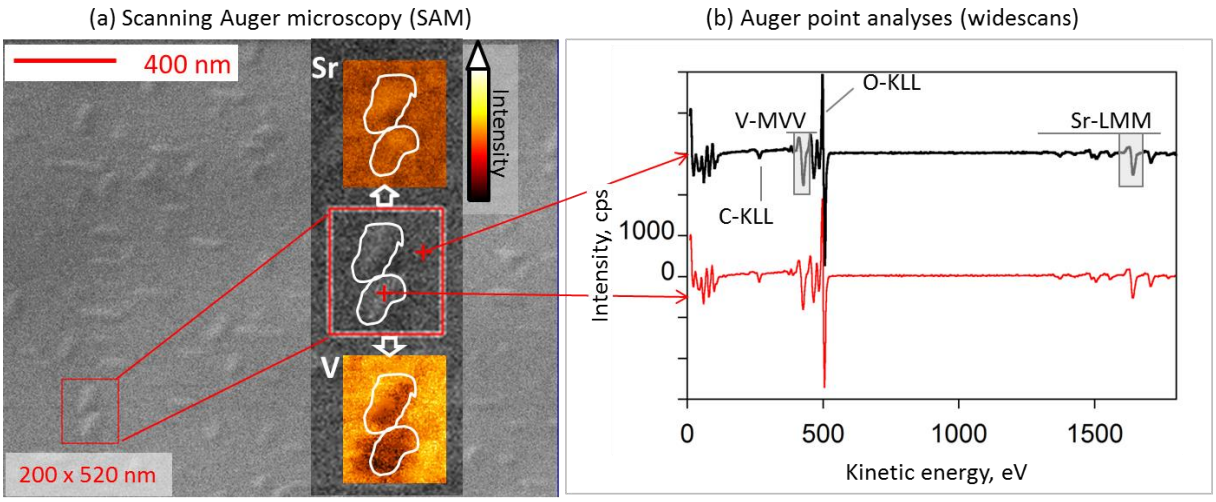

Figure 2. Auger mapping area location on the SE image of SVO film with presence of nanostructures and resulting Sr and V intensities cartographies (a), white figures are guide for eyes, Auger point analyses differentiated widescans acquired on a nanostructure (red) and outside (black) (b). The transitions used for Sr/V ratio evaluation are surrounded.

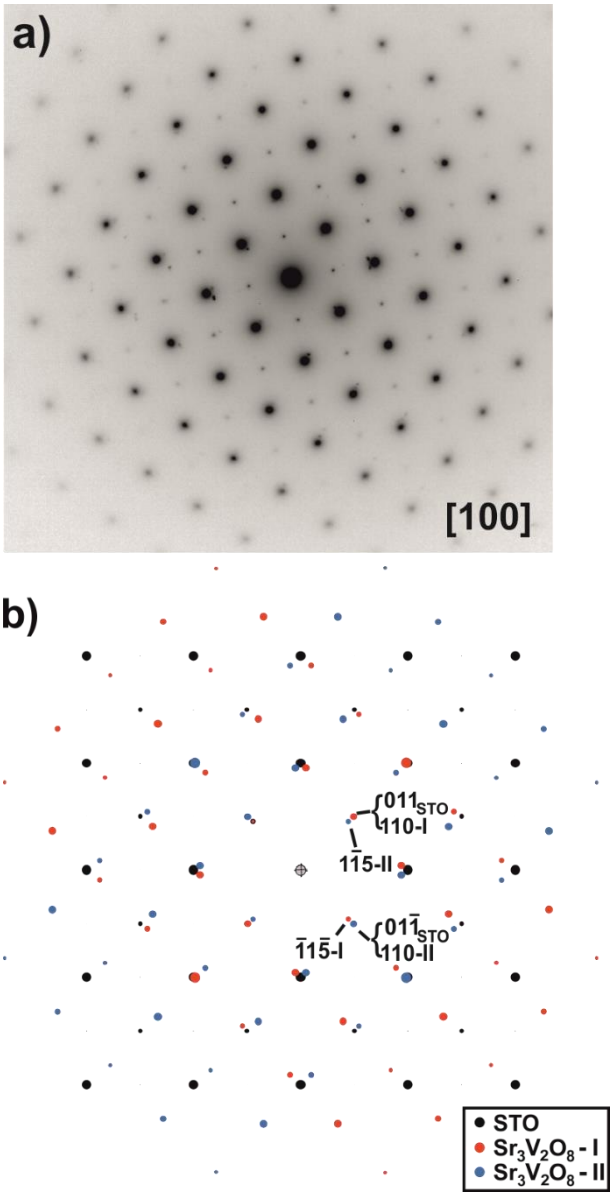

Figure 3. Electron diffraction pattern (EDP) of the STO substrate along the [100] zone axis with reflections of the $Sr_3V_2O_8$ crystallites (a). Simulation of the EDP with the 2 variants of the $Sr_3V_2O_8$ phase and the STO substrate (b).

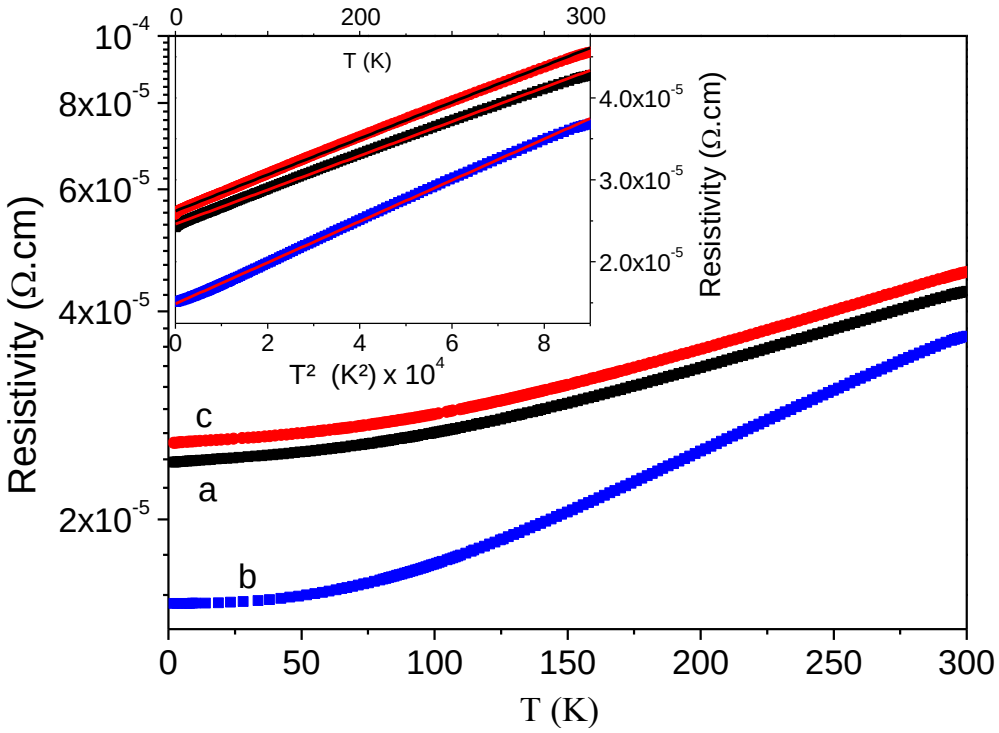

Figure 4. Resistivity curves as function of the temperature for the sample deposited in vacuum, "a", at PO_2= 1.2x10^{-4} Pa, "b", at PO_2= 1.2x10^{-4} Pa followed by a cooling in vacuum, "c". In inset, temperature dependence of resistivity as a function of T^2. The best-fit lines calculated are shown in red for "a" and "b" and in black for "c".

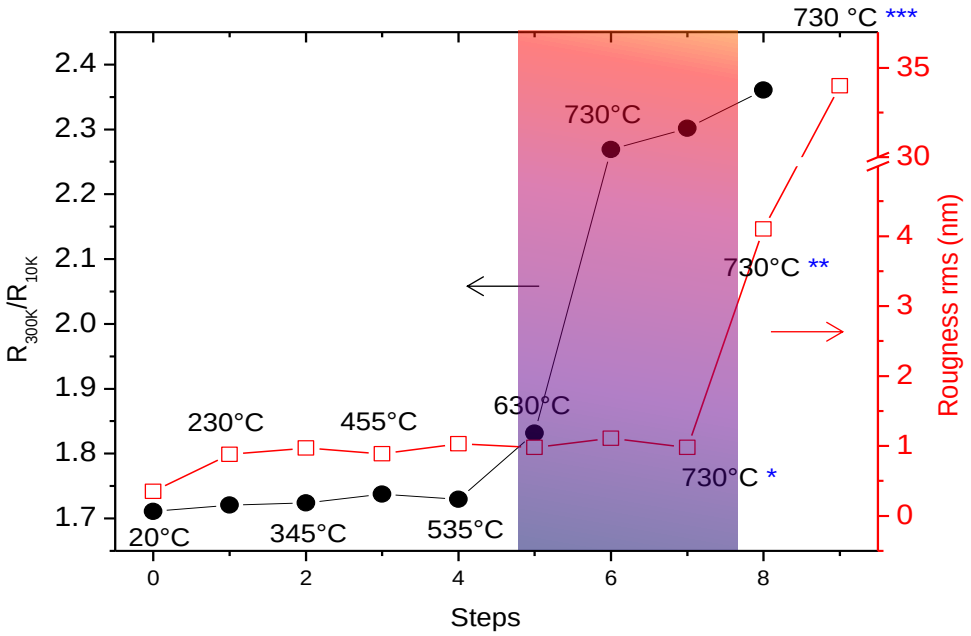

Figure 5. Evolution of R_{300K}/R_{10K} (left axis) and RMS (right axis) for sample similar to "c" grown at PO_2=1.2x10^{-4} Pa and cooled in vacuum (step 0) and after different annealing at 230, 345, 455, 535, 630, 730 °C in 1.2x10^{-4} Pa of PO_2 [steps 1-6], after annealing at 730 °C with PO_2 supply at high temperature * [step 7] and in two higher PO_2 (1x10^{-3} Pa ** and 1x10^{-2} Pa at T=730 °C) *** [steps 8-9].

Table 1. Electrical properties for the three samples "a"," b", "c" as grown and for sample similar to "c" after different annealing (see figure 5 for details). For step 5 to 7, improvement of the ratio $\mathbf{R_{300K}/R_{10K}}$ due to the re-oxygenation without apparition of nanostructures.

Sample/step	ρ_0 ($x10^{-5}\Omega.cm$)	A ($x10^{-10}\,\Omega.cm.K^{-2}$)	R_{300K}/R_{10K}
a	2.46	2.08	1.77
b	1.48	3.10	2.43
c	2.62	2.21	1.76
steps 1 to 4	3.01	2.46	1.71-1.73
step 5	2.58	2.42	1.83
step 6	1.74	2.54	2.27
step 7	1.67	2.50	2.30
step 8	1.58	2.50	2.36